AIAA JOURNAL
Vol. 39, No. 8, August 2001

Large Eddy Simulations of Sound Radiation from Subsonic Turbulent Jets

W. Zhao,* S. H. Frankel,† and L. Mongeau‡
Purdue University, West Lafayette, Indiana 47907

Large eddy simulations (LES) of subsonic turbulent jets, including the near-field flow and far-field sound radiation, were performed using two different subgrid-scale turbulence models. Two different cases were considered. As a validation case, predictions from a Mach 0.9, Reynolds number 3.6×10^3 randomly forced turbulent jet were performed. Both the near-field velocity statistics and far-field sound directivity were found to be in excellent agreement with previous experimental data and direct numerical simulation (DNS) results. The second case involved a Mach 0.4, Reynolds number 5×10^3 harmonically forced jet. Both axisymmetric and azimuthal inlet disturbances were imposed to facilitate detailed comparisons to recent DNS of axisymmetric jet sound, and to highlight the effects of small-scale turbulence. As part of this second case, the validity of Kirchhoff's method for far-field sound prediction was also assessed in conjunction with LES and the effect of the subgrid-scale turbulence model on sound radiation was examined. The sound source location and levels were different between the three-dimensional turbulent jets and similar two-dimensional axisymmetric laminar jets. Far-field sound radiation predictions, obtained using Kirchhoff's method, were in good agreement with the directly predicted LES results. LES predictions obtained with the dynamic Smagorinsky and the dynamic mixed subgrid-scale turbulence models were similar, although the mixed model resulted in higher turbulence and sound levels. The directivity was not uniform as predicted by Lighthill's theory for a fully turbulent jet, but exhibited a preferred radiation angle between 35 and 70 deg in agreement with reported experimental data from an acoustically excited jet.

I. Introduction

SOUND radiation from turbulent shear flows is an important problem for a number of practical engineering applications of interest to the aircraft and automotive industries. Jet noise is also a canonical problem in aeroacoustics. The use of computational fluid dynamics methods to predict noise emission from jets is a very challenging subfield of the discipline of computational aeroacoustics (CAA). One of the more promising CAA techniques for jet noise prediction is the use of large eddy simulation (LES) to predict the near-field flow in conjunction with an acoustic analogy for predicting the far-field sound. There have been several recent studies that have investigated this and other related methods.

Gamet and Estivalezes[1] performed direct numerical simulations (DNS) of the near field of a two-dimensional, axisymmetric supersonic hot jet with Reynolds number Re of 1×10^3 and Mach number M of 2. LES of the near-field of a three-dimensional round jet at the same Mach number, but with $Re = 3 \times 10^4$, were also performed. For both simulations random perturbations were imposed on the inlet velocity profile. Kirchhoff's method was then used to predict the directivity of the radiated sound field from the computed flowfield within the jet. A comparison of the results to experimental data from the literature led to the conclusion that three-dimensional LES predictions yield better agreement than two-dimensional axisymmetric DNS predictions.

Mitchell et al.[2] performed DNS of both the near-field flow and the far-field sound radiated from subsonic and supersonic, two-dimensional, axisymmetric jets. Inlet harmonic forcing was prescribed at the most unstable frequencies of the jet, calculated from a linear stability analysis. For the subsonic case $M = 0.4$, the main source of sound was reported to be vortex pairing. It was concluded that the acoustic source was quadrupole in nature. The predicted acoustic far field was found to agree with predictions from Lighthill's acoustic analogy.

Freund[3,4] performed three-dimensional DNS of a randomly forced round jet at $Re = 3.6 \times 10^3$ and $M = 0.9$ using 25 million grid points. They did not include the far field in their DNS, but instead used the near-field pressure data from the DNS, together with a solution of the wave equation to predict the far-field acoustic pressure. They showed good agreement with experimental data for the mean Mach-number profile and for the directivity of the radiated sound. They also noted that the Lighthill source term had the greatest amplitude near the end of the potential core.

Boersma and Lele[5] conducted three-dimensional LES of a round jet under the same conditions as in Freund.[3] They only included the near field, with 1.5 million grid points. A dynamic Smagorinsky subgrid-scale (SGS) turbulence model was used to close the filtered Navier–Stokes equations. The near-field flow statistics were in good agreement with the DNS results of Freund,[3] but no sound radiation predictions were reported.

Mankbadi et al.[6] studied supersonic jet noise using two-dimensional LES with a nondynamic Smagorinsky SGS model. The computational domain did include part of the acoustic far field. No quantitative comparisons to experimental data were presented. The shape of the sound pressure level contours was sensitive to the type of inflow disturbance specified.

Bogey et al.[7] conducted LES of a Mach 0.9 jet with a Reynolds number of 6.5×10^4. The Smagorinsky SGS model was used. The mean flow and turbulent intensities were in good agreement with experimental data, as well as sound radiation directivity and sound levels.

Recently, Zhao et al.[8] examined the effects of spatial filtering on sound radiation from a subsonic jet by conducting an a priori analysis using DNS results from a two-dimensional, axisymmetric jet. The conditions of Mitchell et al.[2] were reproduced as a means of code validation. The effects of spatial filtering on the Lighthill stress tensor and far-field sound predictions were found to be significant at high frequencies. A SGS sound model was proposed and yielded improved predictions. These findings were hindered by the relatively low-frequency content in a two-dimensional jet. In a three-dimensional turbulent jet the effects of spatial filtering on high-frequency sound are expected to be more pronounced, and the use of a SGS sound model may be better justified.

Received 7 June 2000; presented as Paper 2000-2078 at the AIAA/CEAS 6th Aeroacoustics Conference, Lahaina, HI, 12–14 June 2000; revision received 7 March 2001; accepted for publication 9 March 2001.

*Postdoctoral Researcher, School of Mechanical Engineering.
†Associate Professor, School of Mechanical Engineering. Senior Member AIAA.
‡Associate Professor, School of Mechanical Engineering. Member AIAA.

In the present study three-dimensional LES of sound radiation from subsonic turbulent jets at two different Mach and Reynolds numbers were performed. Efforts were made to include the acoustic far field in the LES domain. A Mach 0.9, $Re = 3.6 \times 10^3$ jet validation case was simulated using random forcing applied at the inflow boundary. The near-field results, including mean velocity and Reynolds-stress profiles, and the far-field results, in particular the sound pressure level (SPL) directivity, were compared with previously available experimental data and DNS results. A Mach 0.4, $Re = 5 \times 10^3$ jet with harmonic inlet forcing, as opposed to random forcing, was used to facilitate comparisons to previous two-dimensional axisymmetric jet noise studies and to highlight the effects of small-scale turbulence. Two different dynamic SGS turbulence models were used, and their impact on the near-field flow statistics and the far-field sound was assessed. The LES-computed far-field sound was compared with predictions using Kirchhoff's method. The directivity of the sound emitted by the jet, as predicted using the hybrid LES–Kirchhoff method, was compared with predictions from Lighthill's theory.

II. Computational Approach

A. Numerical Method

The Favre-filtered compressible Navier–Stokes and energy equations were solved in a cylindrical coordinate system on a three-dimensional grid. Ideal gas behavior was assumed. The governing equations were numerically integrated using a fourth-order Runge–Kutta method for time discretization and a combination of Fourier pseudospectral methods in the azimuthal direction and sixth-order compact finite difference methods in the axial and radial directions for spatial discretization. Explicit fourth-order spatial filtering of the flow variables was used to eliminate high-frequency spurious numerical oscillations.

B. SGS Turbulence Models

Two different compressible SGS turbulence models were used to close the filtered LES equations. The first was the dynamic Smagorinsky model (DSM), and the second was the dynamic mixed model (DMM).[9] The main difference between the two models is that the DMM contains a scale-similarity contribution to the eddy viscosity in addition to the Smagorinsky part. The scale-similarity contribution is expected to decrease the total amount of dissipation provided by the SGS model because it allows for additional backscatter. In what follows, an overbar represents the spatial LES filter, and a tilde represents a density-weight filter. In addition, ρ, u_i, Δ, and S_{ij} represent the density, velocity vector, filter width, and strain-rate tensor, respectively. The two-parameter mixed model for the SGS stress tensor $\tau_{u_i u_j}$ in a compressible flow is given as[9]

$$\tau_{u_i u_j} \equiv \bar{\rho}(\widetilde{u_i u_j} - \tilde{u}_i \tilde{u}_j) \simeq C_{ss}\left(\widetilde{\bar{\rho}\tilde{u}_i \tilde{u}_j} - \widetilde{\bar{\rho}\tilde{u}_i}\,\widetilde{\bar{\rho}\tilde{u}_j}/\bar{\bar{\rho}}\right) - 2C\bar{\rho}\Delta^2|\tilde{S}|\left(\tilde{S}_{ij} - \tfrac{1}{3}\tilde{S}_{kk}\delta_{ij}\right) + \tfrac{2}{3}C_I\bar{\rho}\Delta^2|\tilde{S}|^2\delta_{ij} \tag{1}$$

where the first term on the right-hand side is the scale-similarity part and the second and third terms are the eddy-viscosity parts. C_{ss}, C, and C_I are model coefficients. C_I is assumed to be 0 for the subsonic Mach-number flows in this study. Introducing a test filter, indicated by a caret, whose width is larger than the grid filter and using Germano identity, one can obtain C_{ss} and C using a least-squares approach[10]:

$$C_{ss} = -\frac{\langle M_{ij}L^D_{ij}\rangle\langle M_{mn}N^D_{mn}\rangle - \langle M^2_{ij}\rangle\langle L^D_{mn}N^D_{mn}\rangle}{\langle M_{ij}N^D_{ij}\rangle\langle M_{mn}N^D_{mn}\rangle - \langle M^2_{ij}\rangle\langle N^{D^2}_{mn}\rangle}$$

$$C = -\frac{\langle N^D_{ij}L^D_{ij}\rangle\langle M_{mn}N^D_{mn}\rangle - \langle M_{ij}L^D_{ij}\rangle\langle N^{D^2}_{mn}\rangle}{\langle M_{ij}N^D_{ij}\rangle\langle M_{mn}N^D_{mn}\rangle - \langle M^2_{ij}\rangle\langle N^{D^2}_{mn}\rangle}$$

where $\langle\ \rangle$ represents averaging in the azimuthal direction and the superscript D stands for the deviatoric part of the tensor. L_{ij}, M_{ij}, and N_{ij} are given by

$$L_{ij} = \widehat{\bar{\rho}\tilde{u}_i\tilde{u}_j} - \frac{1}{\hat{\bar{\rho}}}\widehat{\bar{\rho}\tilde{u}_i}\,\widehat{\bar{\rho}\tilde{u}_j} \tag{2}$$

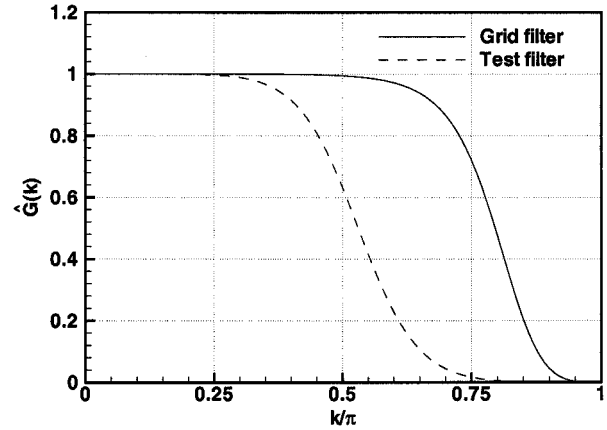

Fig. 1 Fourier transform of the grid and test filter.

$$M_{ij} = -2\hat{\bar{\rho}}\hat{\Delta}^2|\hat{\tilde{S}}|\left(\hat{\tilde{S}}_{ij} - \tfrac{1}{3}\hat{\tilde{S}}_{kk}\delta_{ij}\right) + 2C\widehat{\bar{\rho}\Delta^2|\tilde{S}|\left(\tilde{S}_{ij} - \tfrac{1}{3}\tilde{S}_{kk}\delta_{ij}\right)} \tag{3}$$

$$N_{ij} = \widehat{\bar{\rho}\tilde{\tilde{u}}_i\tilde{\tilde{u}}_j} - \frac{1}{\hat{\bar{\rho}}}\widehat{\bar{\rho}\tilde{\tilde{u}}_i}\,\widehat{\bar{\rho}\tilde{\tilde{u}}_j} \tag{4}$$

For the dynamic Smagorinsky model $C_{ss} = 0$, and

$$C = \frac{\langle L^D_{ij}M_{ij}\rangle}{\langle M_{ij}M_{ij}\rangle} \tag{5}$$

A fourth-order test filter was also applied in the axial and radial directions for the implementation of the dynamic models. The Fourier transforms of the test filter and the filter for numerical stability are shown in Fig. 1. The latter one was also used as the grid filter in the SGS models. The ratio of the test- to grid-filter widths was 1.5. In the azimuthal direction Fourier cutoff filters with the same filter width ratio were used.

C. Flow and Inlet Conditions

For the Mach 0.9 jet the flow conditions were chosen to match the experiment by Stromberg et al.[11] and the DNS by Freund.[3,4] The Reynolds number based on jet nozzle diameter was $Re = 3.6 \times 10^3$. A hyperbolic tangent velocity profile was specified at the inlet:

$$u = \tfrac{1}{2}U_0\{1 - \tanh[(R_0/4\delta_2)(r/R_0) - (R_0/r)]\} \tag{6}$$

where U_0, R_0, and δ_2 are the velocity, radius, and momentum thickness of the jet, respectively. To force the jet, δ_2 was randomly varied in time and azimuthal angle ϕ with a mean value of $0.08R_0$. The maximum amplitude of the variation was about 2%.

For the Mach 0.4 jet the flow conditions were identical to those for axisymmetric jet cases recently reported in the literature.[2,8] Specifically, $M = 0.4$ and $Re = 5 \times 10^3$ based on the jet nozzle diameter. The initial conditions were obtained by solving the parabolic boundary-layer equations with an inlet hyperbolic tangent velocity profile and momentum thickness $\delta_2 = 0.1R_0$ (Ref. 8). Eigenfunctions obtained from an inviscid linear stability analysis based on a numerical solution of Rayleigh's equation for the inlet hyperbolic tangent velocity profile were used to force the jet at the inlet. Three modes were used: the most unstable axisymmetric mode f_0, its subharmonic $\frac{1}{2}f_0$, and a helical mode with an azimuthal wave number $\beta = 1$ at frequency f_0. According to linear stability analysis, $f_0R_0/U_0 = 0.218$, and f_0 was also very close to the most unstable frequency of the helical modes. The inlet disturbance vector φ' can be written as

$$\varphi' = \Re[A_0\hat{\varphi}_0\exp[-i\omega_0 t] + A_1\hat{\varphi}_1\exp[i(-\omega_0 t/2 + 2.7)] + A_h\hat{\varphi}_h\exp[i(-\omega_0 t + \beta\phi)] \tag{7}$$

where $\hat{\varphi}$ is the eigenfunction vector from linear stability theory, normalized such that the maximum magnitude of the axial velocity eigenfunction $|\hat{u}|$ equals 1. $\omega_0 = 2\pi f_0$, $A_0 = 0.0025$, $A_1 = 0.0025$,

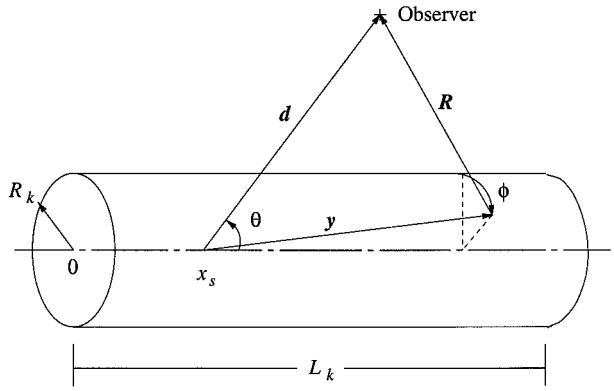

Fig. 2 Domain for Kirchhoff's surface method.

and $A_h = 0.0005$. This disturbance vector was added to the inlet flow variables not otherwise specified by the nonreflecting characteristic boundary condition treatment (to be described). Thus, the amplitude of the helical mode was about 0.1 times that of the sum of the axisymmetric modes. The reason for choosing such a small magnitude helical disturbance was to obtain vortex roll up and pairing, similar to those obtained in previous axisymmetric simulations,[2,8] and small-scale turbulence in the same simulation domain.

D. Kirchhoff Surface Method

The Kirchhoff surface method for predicting far-field sound is based on an analytical formula that relates the far-field sound to integrals over a closed surface that surrounds all acoustic sources. Outside the surface the flow is assumed to be linear, and the acoustic variables, such as pressure and density, satisfy the wave equation. The Kirchhoff surface considered in this report is an open cylindrical surface with radius R_k surrounding the jet, as shown in Fig. 2. x_s, d, Θ, y, R, and ϕ are the source location, the distance between the source and the observer, the angle between the jet axis and the line connecting the source and the observer, the distance between the source and a point on the Kirchhoff surface, the distance between the observer and a point on the Kirchhoff surface, and the azimuthal angle, respectively. Freund et al.[12] suggested that as long as the line between the apparent sound source and the far-field observer intersects the Kirchhoff surface where the acoustic data are available, then errors from truncating the integral will be small. Otherwise errors will be dominant. To reduce the volume of the far field where errors would be expected to dominate, the radius of the Kirchhoff surface should be small, and the length of the surface should be as large as possible.

In the present case the mean velocity in the far field is $U_\infty = 0$. The Kirchhoff–Helmholtz equation relates the temporal Fourier transform of an acoustic variable, say $\hat{\phi}$, to the surface integral of $\hat{\phi}$ and its derivative normal to the surface $\hat{\phi}_n$ and has the following form:

$$\hat{\phi}(\boldsymbol{d}, \omega) = \int_S [\hat{\phi}(\boldsymbol{y})\hat{G}(\boldsymbol{d}-\boldsymbol{y}) - \hat{\phi}_n(\boldsymbol{y})\hat{G}_n(\boldsymbol{d}-\boldsymbol{y})]\,\mathrm{d}S(\boldsymbol{y}) \tag{8}$$

where the Green's function G is

$$G(\boldsymbol{R}) = (1/4\pi R)\exp(i\omega R/c) \tag{9}$$

with c as the sound speed. The integral can be simplified to yield[13]

$$\hat{\phi}(\boldsymbol{d}, \omega) = -\frac{1}{4\pi}\int_S \left[\frac{\hat{\phi}}{d^2}\frac{\partial d}{\partial n} + \frac{\hat{\phi}_n}{d} + \frac{-i\omega}{cd}\hat{\phi}\frac{\partial d}{\partial n}\right]\exp\left(\frac{i\omega R}{c}\right)\mathrm{d}S \tag{10}$$

This is the Kirchhoff formulation for a stationary surface in the frequency domain. It was numerically integrated over the cylindrical surface described using a second-order accurate method.

E. Computational Domain and Details

Nonreflecting characteristic-based boundary conditions were employed together with an extended buffer domain.[14] The buffer domain featured grid stretching and enhanced viscosity to minimize reflections from the boundaries. For the Mach 0.9 jet only the DSM was applied. The computational domain extended $40R_0$ in the axial direction (not including the buffer zone) and $40R_0$ in radial direction. The computational domain was discretized using a nonuniform grid consisting of $400 \times 160 \times 32$ grid points in the axial, radial, and azimuthal directions, respectively. For the Mach 0.4 jet both the DSM and DMM SGS models were used. For the DSM case the domain size was the the same as for the Mach 0.9 case, and the grid size was $320 \times 140 \times 64$. For the DMM case the computational domain was $50R_0$ in axial direction, and the grid size was $400 \times 140 \times 64$. The code employs axial domain decomposition and uses the message-passing-interface libraries for parallel computations. The calculations were performed using the SGI Origin 2000 and IBM SP2 parallel supercomputers. Each LES case required about 4000 CPU hours total on 16 processors.

III. Mach 0.9 Jet

Figure 3 shows contour plots of the magnitude of the instantaneous near-field vorticity and the far-field acoustic pressure p'. The jet transitions to turbulence at around $x^* = 16R_0$. It appears that the dominant sound source is located in this region, which is consistent with the previous DNS results of Freund.[3,4] Figure 4 shows the mean centerline velocity, again in good agreement with the same

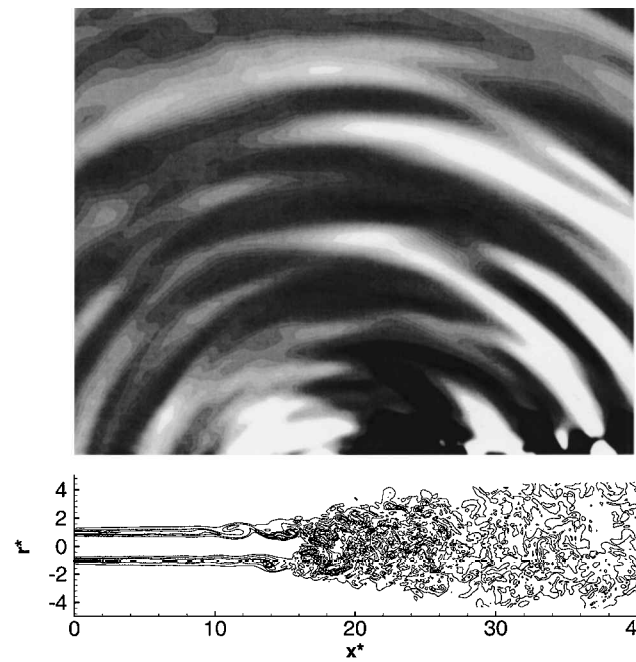

Fig. 3 Instantaneous contour plots of the near-field vorticity magnitude (lower plot) and the far-field acoustic pressure (upper plot). For $|\omega^*|$, MIN = 0.35, MAX = 4.0, and Delta = 0.73; for p', MIN = -2×10^{-4}, MAX = 7×10^{-4}, and Delta = 4.5×10^{-5}.

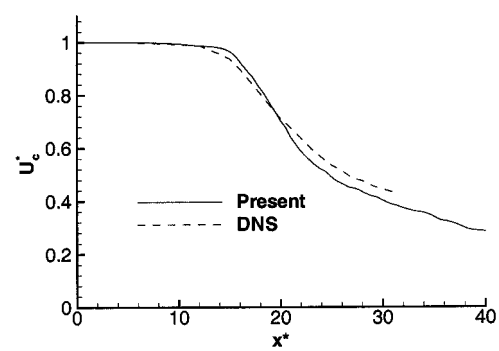

Fig. 4 Centerline mean velocity compared with DNS results.

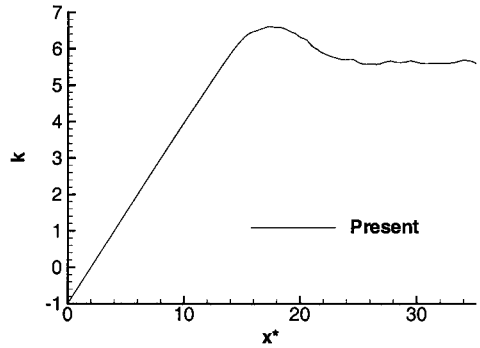

Fig. 5 Decay constant vs axial coordinate.

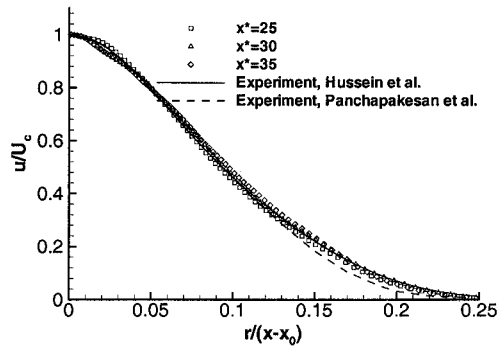

Fig. 6 Radial profiles of mean axial velocity. The experimental profiles are replotted from their curve fits.

earlier DNS results, which were shown to be in excellent agreement with experimental data.[4] The potential core of the jet in the present simulation is slightly longer than that of Ref. 4, and the centerline velocity decreases slightly faster in the early stage of the transition. The reason for those discrepancies is attributed to the inflow conditions. As will be shown in the next section, the inflow forcing has a dramatic effect on the decay of the jet centerline velocity. The decay coefficient of jet, which is defined as

$$k = \frac{U_c(x)}{U_0}\frac{(x - x_0)}{2R_0} \tag{11}$$

is shown in Fig. 5. $U_c(x)$ is the centerline velocity. x_0 is the so-called virtual origin of the jet, chosen to be $1.0R_0$. Previous experiments on low-Mach-number jets have shown that k becomes a constant when the jet is fully developed, with a value is in the range between 5.7 and 6.1 (Ref. 15). The decay constant in the present simulations is about 5.7, slightly smaller than the value of 5.8 predicted by the DNS results of Ref. 4. The mean velocity profiles at three axial positions are shown in Fig. 6. Also shown for comparison in the figure are experimental results for low-Mach-number jets reported by Panchapakesan and Lumley[16] and Hussein et al.[17] The agreement is excellent despite the large differences between the present simulation and the experiments for the Mach and Reynolds numbers. Following Freund,[4] Fig. 7 shows the profiles of the Reynolds-stress components, normalized by U_c^2. The agreement between the simulation and the experimental data is reasonable. Finally, a comparison of the SPL obtained in the present simulation and experimental data from Stromberg et al.,[11] Mollo-Christensen et al.,[18] and Lush[19] is shown in Fig. 8. Again, reasonable agreement was obtained. The good agreement between numerical results and data for both the near-field flow and far-field sound radiation confirms similar results obtained in the DNS comparison of Freund[3,4] and provides evidence supporting the validity of the numerical procedures used here.

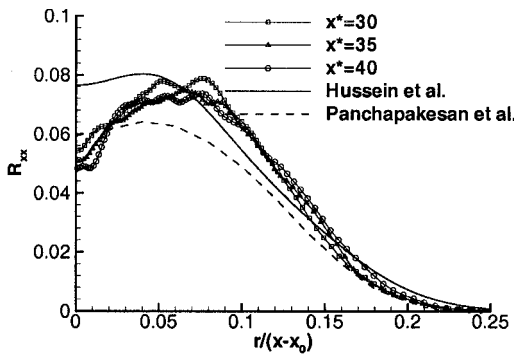

R_{xx}

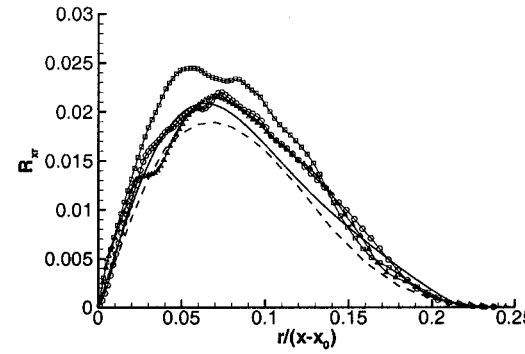

R_{xr}

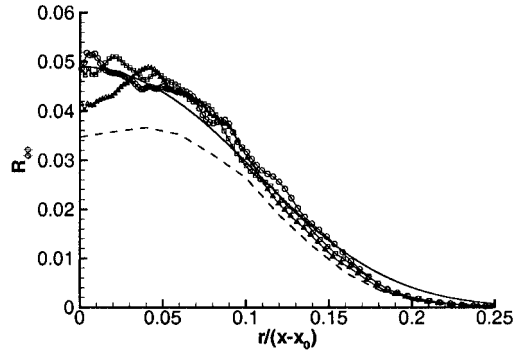

$R_{\phi\phi}$

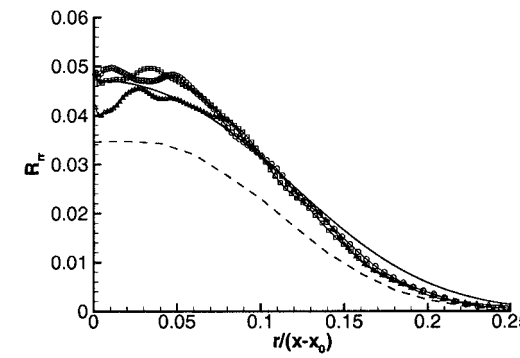

R_{rr}

Fig. 7 Radial profiles of components of the Reynolds-stress tensor. The experimental profiles are replotted from their curve fits.

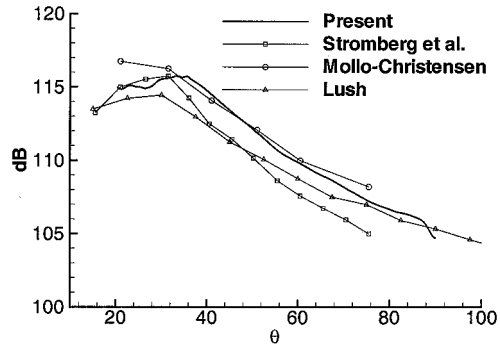

Fig. 8 SPL directivity compared with experimental data.

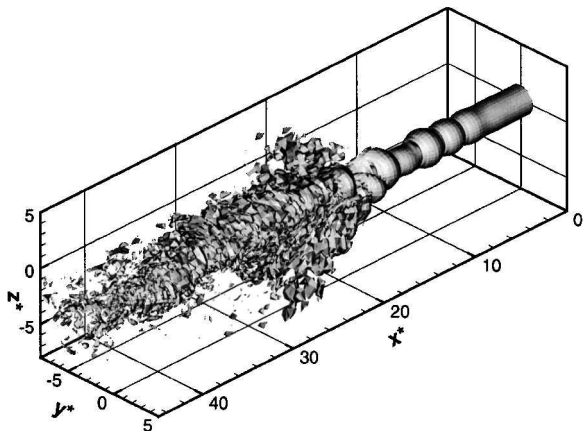

Fig. 9 Instantaneous surface of isovorticity magnitude from the case using the DMM subgrid-scale model. The magnitude of the vorticity $|\omega^*|$ is 0.6. Only every other point in each direction is used to construct the plot.

IV. Mach 0.4 Jet

A. Near-Field Flow Analysis

To visualize the flow structure and examine the effects of the forcing employed, an instantaneous surface of isovorticity magnitude is shown in Fig. 9 from the LES using the DMM. Similar results were obtained using the DSM. Recall that the magnitude of the axisymmetric instability modes ($\beta = 0$) used to force the jet at the inlet boundary was 10 times larger than that of the helical mode ($\beta = 1$). In the region just downstream of the inlet, the axisymmetric mode is dominant, and the vortex ring development is quite similar to that observed in previous axisymmetric simulations.[2,8] The nonsymmetric structures emerge at $x^* \approx 14$. Beyond this axial location the large-scale vortical structures break up, and the flow transitions to turbulence very rapidly. The effect of the helical modes on the axisymmetric vortices can also be seen in Fig. 10, where instantaneous contours of the azimuthal component of vorticity at four different axial location are shown. At the position $x^* = 10.9$ the vorticity is almost axisymmetric. At the positions $x^* = 14.1$ and $x^* = 17.2$ the vorticity is no longer axisymmetric and has developed an asymmetric lobed structure. At the location $x^* = 20.3$ the large-scale vortical structures break up into smaller-scale vorticity.

LES predictions for the mean centerline axial velocity are plotted vs axial location in Fig. 11 for both SGS models. Also shown for comparison is the same quantity from the two-dimensional axisymmetric DNS results of Zhao et al.[8] The three simulations are in excellent agreement with each other in the region $0 \leq x^* \leq 16$, where the flow is laminar and almost axisymmetric as a result of the imposed forcing. Beyond this region the centerline velocity in the three-dimensional turbulent jet continues to decrease, whereas that of the axisymmetric jet increases slightly and then remains almost constant. In the region $21 \leq x^* \leq 22$ a rapid decrease in the centerline velocity is observed for both the DSM and DMM simulations. This rapid decrease in the centerline velocity is attributed to the helical mode excitation introduced at the inlet boundary, which grows downstream as evidenced by the asymmetric lobed structure already discussed. This flow behavior apparently enhances the

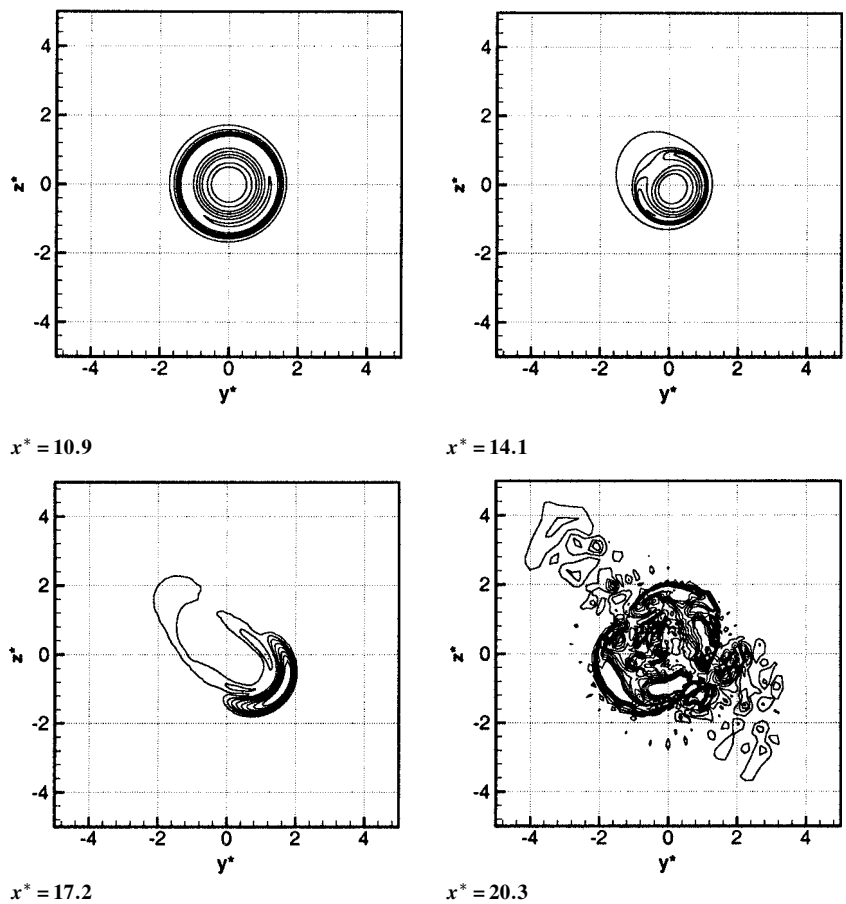

Fig. 10 Contour plots of the azimuthal component of the vorticity in the cross section at different axial locations.

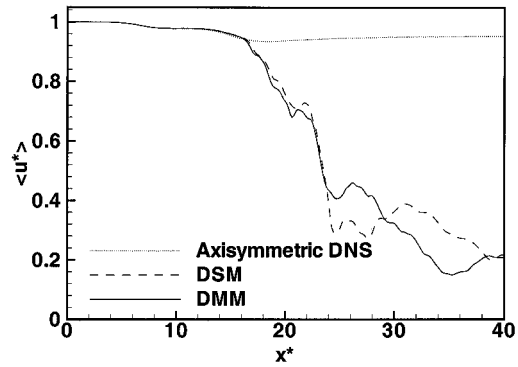

Fig. 11 Time-averaged axial velocity vs axial distance along the centerline.

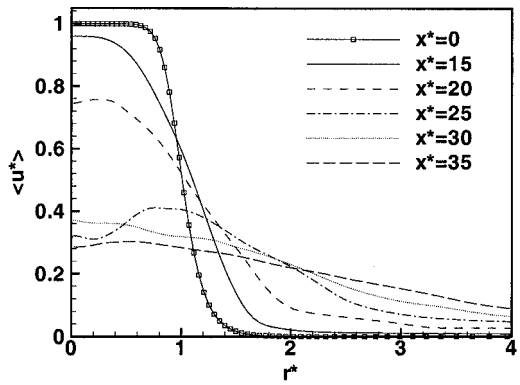

DSM

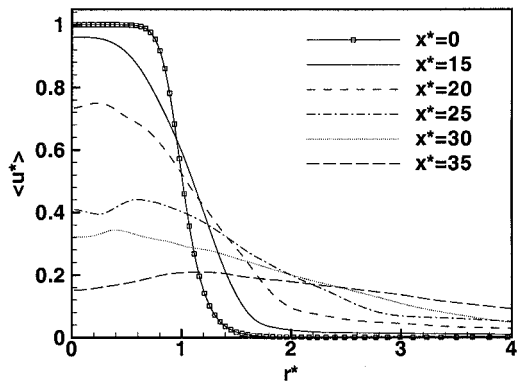

DMM

Fig. 12 Mean axial velocity profiles at different axial locations.

mixing of the jet. This enhancement of jet mixing through helical mode excitation, along with the associated rapid decrease of centerline velocity, was also recently observed by other researchers.[20] This is in constrast to the relatively smooth decay of the centerline velocity observed in the randomly forced Mach 0.9 case in Fig. 4. Discrepancies between the DSM and DMM simulations may be observed in the downstream region of the jet. Further evidence can be seen in Fig. 12, which compares the mean velocity profiles predicted by the two simulations.

Radial profiles of components of the Reynolds-stress tensor at different axial locations are shown in Fig. 13. The results are in qualitative agreement with the DNS results of Freund[3,4] and the LES results of Boersma et al.[5] The Reynolds stresses reach their maximum value in the transition region ($x^* \approx 20$) and then begin to diffuse and dissipate. The component $R_{\phi\phi}$ remains almost zero until $x^* = 15$ because the axisymmetric excitation mode at the inlet is dominant and the azimuthal excitation mode is small by design. Also, note that the three normal stress components predicted in the DMM simulation are slightly larger than those predicted by the DSM simulation around the transition region. Because of the specific inlet forcing employed in these simulations, quantitative comparisons to previous experimental data or DNS results could not be made.

Contour plots of the mean turbulent kinetic energy (TKE) k computed as $\frac{1}{2}\langle u_i' u_i' \rangle$, where $u_i' = \tilde{u}_i - \langle \tilde{u}_i \rangle$ (the asterisk, denoting nondimensionalization, was dropped for clarity and the angle brackets represent time averages), obtained from the two LES cases, are shown in Fig. 14. The contours are qualitatively very similar. These results are also similar to those obtained by Freund.[3] To quantify the turbulence levels, $\sqrt{(2k)}$ is computed along the centerline and plotted as a function of axial distance in Fig. 15. The peak turbulence level occurs near the transition location and is approximately 20% greater with DMM than with DSM. This trend is attributed to the more dissipative nature of DSM as compared to DMM.[21,22]

Spectra of the azimuthal TKE at $r^* = 0.5$ and different axial locations are shown in Fig. 16. As expected, the TKE levels near the inlet are relatively low. Downstream of the transition location, the spectra predicted using the DMM contain more energy at higher wave numbers than in the DSM case. This is again consistent with recent observations that the mixed model is less dissipative than the Smagorinsky model.[21,22]

B. Far-Field Sound Radiation Analysis

A contour plot showing an azimuthal slice of the instantaneous near-field vorticity magnitude, together with the far-field dilatation, is shown in Fig. 17 for the DMM SGS model. The results are qualitatively similar for the DSM case. The acoustic waves appear to be emanating from the transition region, consistent with the Mach 0.9 case and previously reported findings.[3,4,23] This is in contrast with the two-dimensional axisymmetric jet, where the sound source was observed to be the vortex pairing region.[2,8] The magnitude of the dilatation in the far field (which is considered a measure of the sound level) is one order of magnitude higher for the turbulent jet than in the axisymmetric jet of Zhao et al.[8]

In the lower-right-hand corner of the dilatation contour plot, the dilatation magnitude is considerably higher than elsewhere. The helical modes excited at the inlet of the jet cause it to expand more abruptly just downstream of the transition region than for the case of a randomly forced jet. Thus, this area is affected by the near field of the jet, where the turbulent fluctuations dominate the acoustic fluctuations. Nevertheless, this region does not appear to make a significant contribution to the far-field sound radiation because the sound radiation pattern just outside this region is very similar to rest of the far field. Those near-field effects were not observed in the randomly forced Mach 0.9 jet already discussed.

Goldstein[23] describes Lighthill's mechanism for sound radiation from turbulent eddies as similar in behavior to a large number of random quadrupoles, which are moving downstream at some turbulence convection velocity. Lighthill's result[24] for the far-field acoustic intensity $I = p'^2_{\text{rms}}/\rho_0 c_0$, generated by a turbulent flow and corrected later by Ffowcs Williams[25] for applications to noise radiation from a turbulent jet, can be written in dimensional form as

$$I(\theta) \sim \frac{f(\theta)}{(1 - M_c \cos\theta)^5} \tag{12}$$

where $f(\theta)$ is the directivity of the unconvected random distribution of quadrupoles at rest, θ is the angle between the jet axis and the line connecting the jet exit and the observer, and M_c is the convection speed of the quadrupoles divided by the speed of sound. Typically, $f(\theta)$ is assumed to be uniform, consistent with the assumption that turbulent jet noise is generated by a large number of random quadrupoles. Experimental measurements confirm this uniform directivity for low-Mach-number jets with low convection speed.[19] To compare predictions from the present simulations to Lighthill's theory and experimental data, a Kirchhoff surface was used to predict the sound level in the jet far field. Although the LES computational domain in this study does reach the far field, it is still not large enough to compute the directivity. The Kirchhoff method was first validated by comparing its predictions with directly computed results. Three Kirchhoff surfaces are employed for this purpose with the source location chosen as $x_s = 0$ (jet inlet) and radii of $R_k = 10R_0$, $15R_0$, and $20R_0$, respectively.

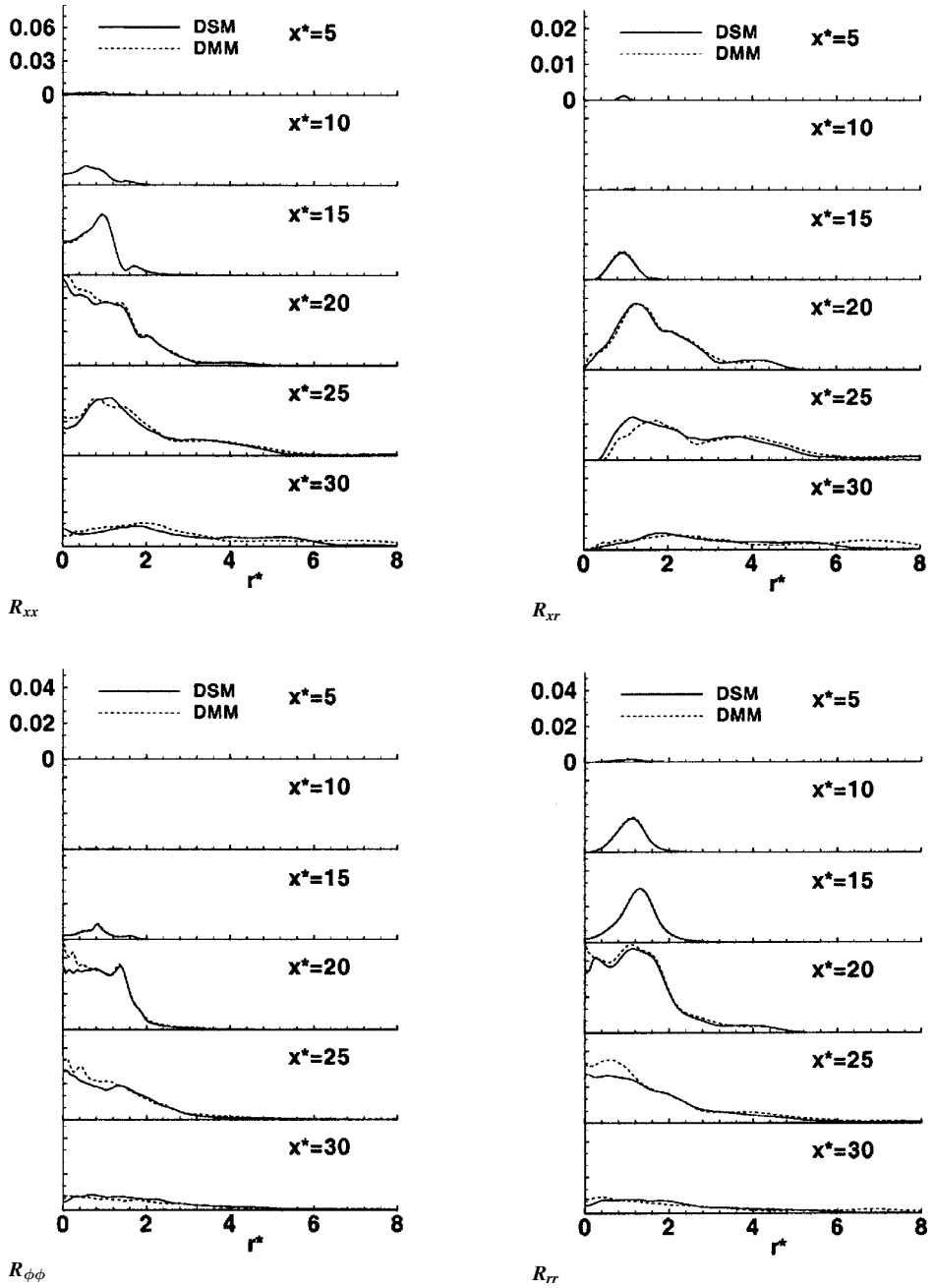

Fig. 13 Radial profiles of key Reynolds-stress tensor components $R_{ij} = \langle u_i' u_j' \rangle$ at different axial positions.

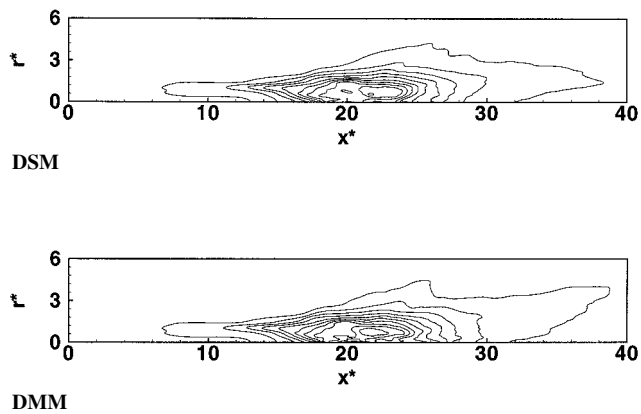

Fig. 14 Contour plot of mean turbulent kinetic energy averaged in the cross section: MIN = 0.005, MAX = 0.065, and Delta = 0.004.

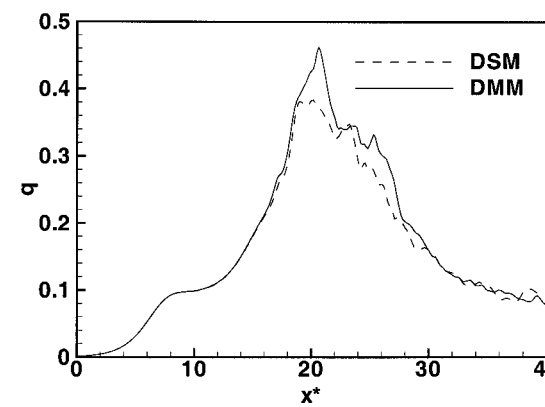

Fig. 15 Plot of $q = \sqrt{(2k)}$ vs axial distance along the centerline.

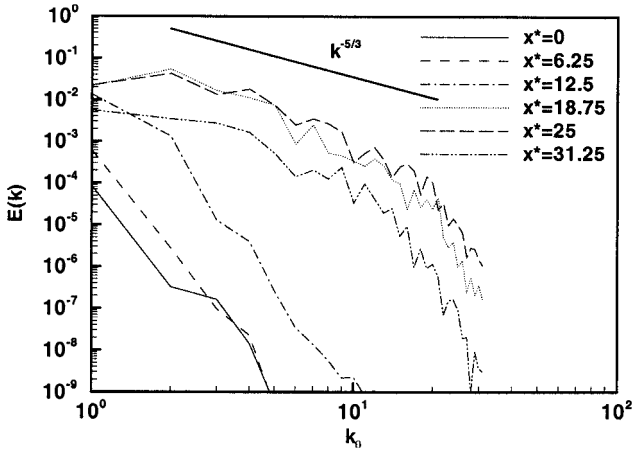

DSM

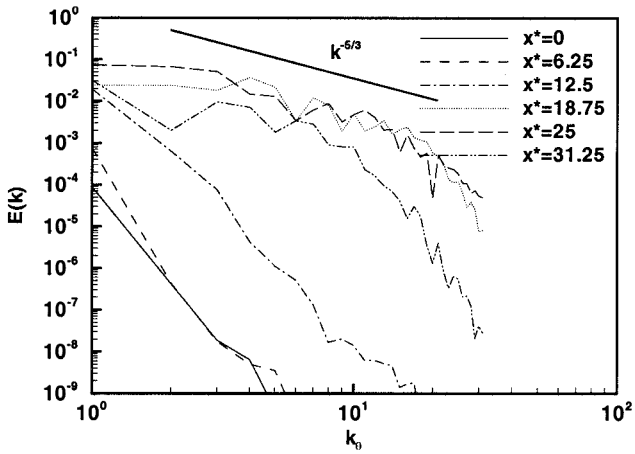

DMM

Fig. 16 Azimuthal wave-number-frequency spectrum of the turbulent kinetic energy at different axial positions at $r^* = 0.5$.

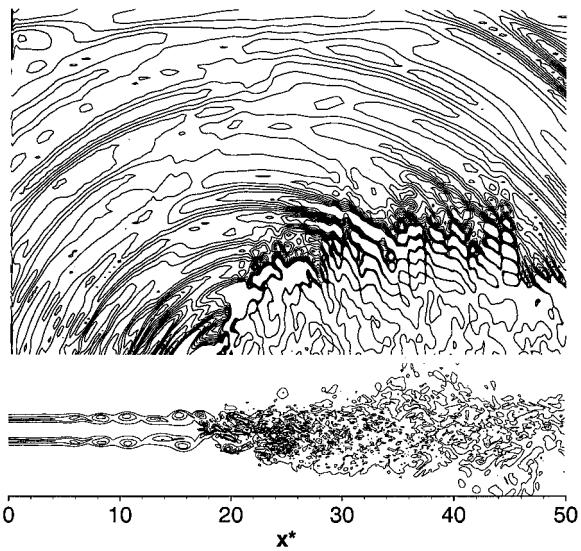

Fig. 17 Instantaneous contour plots of the near-field vorticity magnitude (lower plot) and the far-field dilatation (upper plot) from the case using the DMM subgrid-scale model. For $|\omega^*|$, MIN = 0.3, MAX = 4.3, and Delta = 0.4; for Θ^*, MIN = -3×10^{-5}, MAX = 3×10^{-5}, and Delta = 6×10^{-6}.

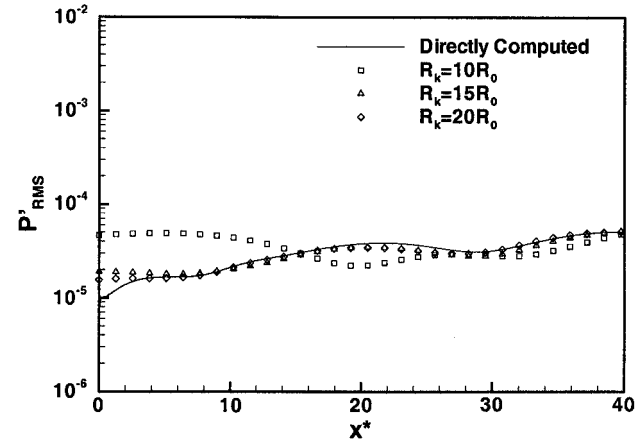

DSM

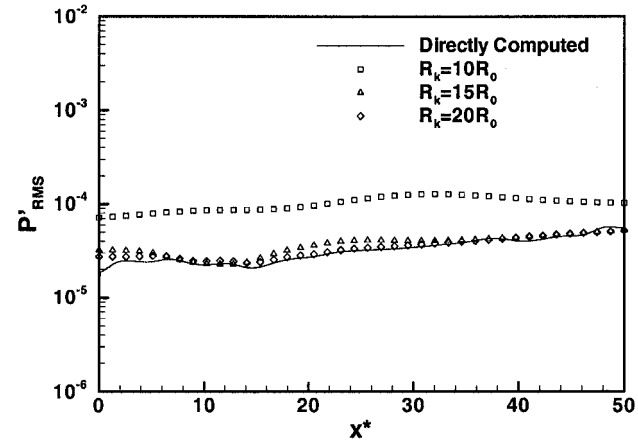

DMM

Fig. 18 Root-mean-square acoustic pressure along the line, $r^* = 30$, $\phi = 0$ as predicted by LES and the Kirchhoff method.

The comparison between the Kirchhoff prediction and the direct computation of the rms acoustic pressure p'_{rms} is shown in Fig. 18. Here, p'_{rms} is calculated by summing the Fourier components at each frequency:

$$p'_{\text{rms}} = \left[\sum_{n=1}^{N} \left(\rho_\infty c_\infty^2 \frac{4|\hat{\Theta}_n|}{n\omega_0} \right)^2 \right]^{\frac{1}{2}} \tag{13}$$

where $\omega_0 = 2\pi f_0$ and N is chosen to be 20, which corresponds to the frequency $5f_0$ and the highest frequency acoustic wave resolved in the simulation (approximately six grid points per wavelength at this frequency). The agreement is excellent for the Kirchhoff radius $R_k = 20R_0$.

The Kirchhoff surface with radius $R_k = 20R_0$ was then used to predict the directivity at a distance of $240R_0$ from the nozzle. The results are plotted in Fig. 19 along with Lighthill's theory of subsonic jet noise [Eq. (12) with $M_c = 0.65M_0$)]. Figure 19 shows that the sound intensity predicted with DMM is higher than that predicted with DSM, which is consistent with the fact that the DMM predicts a higher turbulence intensity. The theory predicts a fairly uniform directivity, while the LES predictions are nonuniform. Specifically, the DMM predictions show a preferred direction for sound radiation in the range between 35 and 70 deg above the jet axis. The preferred sound radiation angle is believed to be related to the harmonic excitation at the inlet. This is in agreement with that reported by Kibens,[26] who measured far-field directivity patterns in acoustically excited low subsonic turbulent jets and also observed a preferred directivity between 35 and 65 deg with respect to the jet axis.

Because of harmonic inlet forcing imposed in the numerical simulations, the jet exhibits organized toroidal vortical structures in the pretransitional region and randomized small-scale turbulence downstream of the transitional region. The transition is caused by a

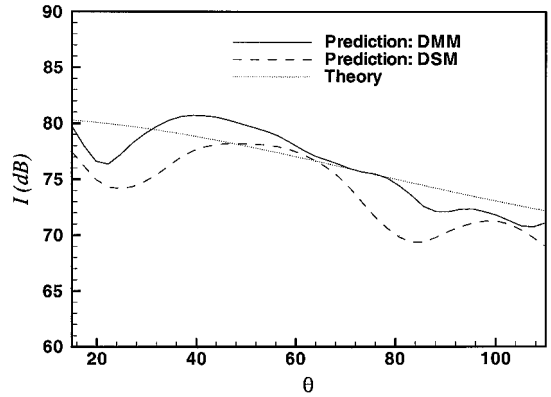

Fig. 19 Predicted jet sound directivity compared with Lighthill's theory.

secondary instability, which develops as a result of the azimuthal forcing exciting helical modes and producing smaller-scale azimuthal lobes (see discussion in Ref. 23). The toroidal vortices are convected at subsonic speed. These would be very poor sound radiators if the flow were laminar throughout the entire domain. When the jet breaks up, however, the well-organized train of toroidal vortices abruptly ends and is replaced by random flow structures. The wavy toroidal motion causes radial particle velocity waves, which propagate at subsonic speeds in the shear layers. The point of transition between the unstable laminar shear layer and the more turbulent part of the jet acts as an edge or a point where coherent interferences in the radiation process are interrupted. At the discontinuity there are no more destructive interferences between dipole source regions in the wavy part of the flow, causing enhanced radiation. The acoustic waves accordingly appear to be emitted from the point of transition, and the preferred radiation angles could be explained by the sound radiation pattern produced when a bending wave impinges on the edge of a flexible plate (see Fig. 4.4.4 in Howe[27]). As mentioned, this preferred radiation pattern is consistent with the experimental data of Kibens.[26]

V. Conclusions

Predictions of the near-field flow and the far-field sound radiation for two subsonic turbulent jets were obtained using the large eddy simulation technique. The axial location of the main sound source in both jets appeared to coincide with the region where the jet transitions from large-scale organized vortical structures to small-scale turbulence. This is in contrast to previous two-dimensional axisymmetric laminar jet simulations, where the main sound source location corresponded to the vortex pairing region. Also, the sound levels were higher in the turbulent jets as compared to the two-dimensional axisymmetric jet. The results of the randomly forced Mach 0.9 jet were in good agreement with the available experimental data and DNS results, which provides a validation of the numerical methods used. For the harmonically forced Mach 0.4 jet, the use of two different subgrid-scale turbulence models resulted in different turbulence and sound levels but in similar flow and sound radiation patterns. Far-field sound predictions obtained using the Kirchhoff method were found to be in reasonable agreement with the directly computed sound. The sound directivity predicted using the Kirchhoff method was also in good quantitative agreement with experimental measurements and acoustic theory for a fully turbulent jet, but exhibited a nonuniform directivity with a preferred radiation angle range in agreement with experimental measurements from an acoustically excited jet. The directivity pattern was explained using acoustic scattering of flexural waves at edges.

Acknowledgments

This work was supported by Research Grant 5 RO1 DC03577-02 from the National Institute of Deafness and Other Communication Disorders, National Institutes of Health. Supercomputer time on the Origin 2000 was provided by the National Center for Supercomputing Applications under Grant CTS980030N. The IBM SP2 was available at Purdue University. The authors thank J. B. Freund at the University of California, Los Angeles, for making a copy of his soon-to-appear *Journal of Fluid Mechanics* paper available to us.

References

[1]Gamet, L., and Estivalezes, J. L., "Application of Large-Eddy Simulation and Kirchoff Method to Jet Noise Prediction," *AIAA Journal*, Vol. 36, No.12, 1998, pp. 2170–2178.

[2]Mitchell, B. E., Lele, S. K., and Moin, P., "Direct Computation of the Sound Generated by Vortex Pairing in an Axisymmetric Jet," *Journal of Fluid Mechanics*, Vol. 383, 1999, pp. 113–142.

[3]Freund, J. B., "Acoustic Sources in a Turbulent Jet: A Direct Numerical Simulation Study," AIAA Paper 99-1858, June 1999.

[4]Freund, J. B., "Noise Sources in a Low-Reynolds-Number Turbulent Jet at Mach 0.9," *Journal of Fluid Mechanics* (to be published).

[5]Boersma, B. J., and Lele, S. K., "Large Eddy Simulation of a Mach 0.9 Turbulent Jet," AIAA Paper 99-1874, June 1999.

[6]Mankbadi, R. R., Shih, S. H., Hixon, R., and Povinelli, L. A., "Direct Computation of Jet Noise Produced by Large-Scale Axisymmetric Structures," *Journal of Propulsion and Power*, Vol. 16, No. 2, 2000, pp. 207–215.

[7]Bogey, C., Bailly, C., and Juve, D., "Computation of Sound Radiated by a 3D Jet Using Large Eddy Simulation," AIAA Paper 2000-2009, June 2000.

[8]Zhao, W., Frankel, S. H., and Mongeau, L., "Effects of Spatial Filtering on Sound Radiation from a Subsonic Axisymmetric Jet," *AIAA Journal*, Vol. 38, No. 11, 2000, pp. 2032–2039.

[9]Salvetti, M., and Banerjee, S., "A Priori Tests of a New Dynamic Subgrid-Scale Model for Finite-Difference Large-Eddy Simulations," *Physics of Fluids*, Vol. 7, No. 11, 1995, pp. 2831–2847.

[10]Lilly, D. K., "A Proposed Modification of the Germano Subgrid-Scale Closure Model," *Physics of Fluids A*, Vol. 4, No. 3, 1992, pp. 633–635.

[11]Stromberg, J. L., McLaughlin, D. K., and Troutt, T. R., "Flow Field and Acoustic Properties of a Mach Number 0.9 Jet at a Low Reynolds Number," *Journal of Sound and Vibration*, Vol. 72, No. 2, 1980, pp. 159–176.

[12]Freund, J. B., Lele, S. K., and Moin, P., "Calculation of the Radiated Sound Field Using an Open Kirchhoff Surface," *AIAA Journal*, Vol. 34, No. 5, 1996, pp. 909–916; also AIAA Paper 95-061, June 1995.

[13]Lyrintzis, A. S., "Review: The Use of Kirchhoff's Method in Computational Aeroacoustics," *Journal of Fluids Engineering*, Vol. 116, No. 4, 1994, pp. 665–675.

[14]Poinsot, T., and Lele, S., "Boundary Conditions for Direct Simulations of Compressible Viscous Flows," *Journal of Computational Physics*, Vol. 101, 1992, p. 104.

[15]Boersma, B. J., Brethouwer, G., and Nieuwstadt, F. T. M., "A Numerical Investigation of the Effect of Inflow Conditions on the Self-Similar Region of a Round Jet," *Physics of Fluids*, Vol. 10, No. 4, 1998, pp. 899–909.

[16]Panchapakesan, N. R., and Lumley, J. L., "Turbulence Measurements in Axisymmetric Jets of Air and Helium. Part 1. Air Jets," *Journal of Fluid Mechanics*, Vol. 246, 1993, pp. 193–223.

[17]Hussein, H. J., Capp, S. P., and George, W. K., "Velocity Measurements in a High-Reynolds-Number, Momentum-Conserving Axisymmetric, Turbulent Jet," *Journal of Fluid Mechanics*, Vol. 258, 1994, pp. 31–75.

[18]Mollo-Christensen, E., Koplin, M. A., and Martucelli, J. R., "Experiments on Jet Flows and Jet Noise Far-Field Spectra and Directivity Patterns," *Journal of Fluid Mechanics*, Vol. 18, 1964, pp. 285–301.

[19]Lush, P. A., "Measurements of Subsonic Jet Noise and Comparison with Theory," *Journal of Fluid Mechanics*, Vol. 46, 1971, pp. 477–500.

[20]Hilgers, A., "Parameter Optimization in Jet Flow Control," Center for Turbulence Research Annual Research Brief, Stanford Univ., Stanford, CA, 1999.

[21]Akhavan, K., Ansari, A., Kang, S., and Mangiavacchi, N., "Subgrid-Scale Interactions in a Numerically Simulated Planar Turbulent Jet and Implications for Modeling," *Journal of Fluid Mechanics*, Vol. 408, 2000, pp. 83–129.

[22]Meneveau, C., and Katz, J., "Scale-Invariance and Turbulence Models for Large Eddy Simulation," *Annual Review of Fluid Mechanics*, Vol. 32, 2000, pp. 1–32.

[23]Goldstein, M. E., "Aeroacoustics of Turbulent Shear Flows," *Annual Review of Fluid Mechanics*, Vol. 16, 1984, pp. 263–285.

[24]Lighthill, M. J., "On Sound Generated Aerodynamically; I. General Theory," *Proceedings of the Royal Society of London*, Vol. A211, 1952, pp. 564–587.

[25]Ffowcs Williams, J. E., "The Noise from Turbulence Convected at High Speed," *Philosophical Transations of the Royal Society of London*, Vol. 248, No. 267, 1963, p. 147.

[26]Kibens, V., "Discrete Noise Spectrum Generated by an Acoustically Excited Jet," *AIAA Journal*, Vol. 18, No. 2, 1980, pp. 434–441.

[27]Howe, M. S., *Acoustics of Fluid-Structure Interactions*, Cambridge Univ. Press, Cambgrid, England, U.K., 1998.

K. Kailasanath
Associate Editor